

Widespread Methanol Emission from the Galactic Center

F. Yusef-Zadeh¹, W. Cotton², S. Viti³, M. Wardle⁴ and M. Royster¹

¹*Department of Physics and Astronomy, Northwestern University, Evanston, IL 60208*

²*National Radio Astronomy Observatory, Charlottesville, VA 22903*

³*Department of Physics and Astronomy, University College London, Gower St. London, WC1E 6BT, UK*

⁴*Department of Physics & Astronomy, Macquarie University, Sydney NSW 2109, Australia*

ABSTRACT

We report the discovery of a widespread population of collisionally excited methanol $J = 4_{-1}$ to 3_0 E sources at 36.2 GHz from the inner $66' \times 18'$ (160×43 pc) of the Galactic center. This spectral feature was imaged with a spectral resolution of 16.6 km s^{-1} taken from 41 channels of a VLA continuum survey of the Galactic center region. The revelation of 356 methanol sources, most of which are maser candidates, suggests a large abundance of methanol in the gas phase in the Galactic center region. There is also spatial and kinematic correlation between SiO (2–1) and CH₃OH emission from four Galactic center clouds: the +50 and +20 km s^{-1} clouds and G0.13-0.13 and G0.25+0.01. The enhanced abundance of methanol is accounted for in terms of induced photodesorption by cosmic rays as they travel through a molecular core, collide, dissociate, ionize, and excite Lyman Werner transitions of H₂. A time-dependent chemical model in which cosmic rays drive the chemistry of the gas predicts CH₃OH abundance of 10^{-8} to 10^{-7} on a chemical time scale of 5×10^4 to 5×10^5 years. The average methanol abundance produced by the release of methanol from grain surfaces is consistent with the available data.

Subject headings: ISM: clouds — molecules — structure Galaxy: center

1. Introduction

Large scale molecular line surveys of the inner few hundred pc of the Galaxy, also known as the central molecular zone (CMZ), have detected emission lines from a wide array

of molecular species formed in gas phase (e.g., H_3^+ , CO, CS, HCO^+ , N_2H^+) and grain-surface (e.g., SiO, CH_3OH and NH_3) chemistry (Martin-Pintado et al. 1997; Martin et al. 2004; Oka et al. 2005; Riquelme, et al. 2010; Jones et al. 2012). What is interesting about these results is that the gas characteristics are similar to those of hot cores associated with protostars and yet the distribution of molecular gas is widespread over a few hundred parsecs with a few isolated pockets of star formation such as Sgr B2. The gas in the Galactic center has a higher temperature than the dust temperature $\leq 30\text{K}$ (e.g., Fig. 3 of Molinari et al. 2011). This characteristic of the warm gas is hard to explain if the hot cores are heated by high mass protostars throughout the population of Galactic center molecular clouds. To investigate the chemistry of the gas in the CMZ, we carried out a high resolution survey of methanol emission from the inner $66' \times 18'$ of the Galactic center.

Here we report discovery of a large population of collisionally excited methanol $J = 4_{-1}$ to 3_0 E emission at 36.2 GHz. Class I methanol masers are collisionally pumped and are generally correlated with outflows in star forming sites (e.g., Voronkov et al. 2006). Given the pervasive distribution of detected maser candidates, we suggest instead that enhanced abundance of methanol is produced globally by the interaction between enhanced cosmic rays and molecular gas in the CMZ.

2. Observations and Data Reduction

The maser observations were conducted with the the K. Jansky Very Large Array (VLA) of the National Radio Astronomy Observatory¹ (NRAO) in its C configuration as part of a continuum survey in which one subband was centered on the rest frequency of the rotational class I methanol masers (36.169265 GHz). This subband had 64×2 MHz channels giving a velocity resolution of $\approx 16.6 \text{ km s}^{-1}$. Each of the ≥ 900 single snapshot pointings were imaged independently and the results combined in a linear mosaic. These observations were made in six sessions between 2012 February 21 and 2012 March 10 under project code 12-120A. J1744-3116 was used as the phase calibrator and 3C286 was used as the photometric and bandpass calibrator with an assumed flux of 1.70 Jy and an uncertainty of 5%. Using the Obit package², calibration, editing and imaging were done on each session independently and consisted of determining first instrumental group delay offsets from observations of 3C286 and J1744-3116, and applying to all data. The methanol features were much narrower in

¹The National Radio Astronomy Observatory is a facility of the National Science Foundation, operated under a cooperative agreement by Associated Universities, Inc.

²<http://www.cv.nrao.edu/bcotton/~Obit.html>

frequency than a channel, so the stronger features gave significant Gibbs ringing in frequency due to the limited range of lags used by the correlator. The resolution is approximately $1.8'' \times 0.7''$ with RMS noise ≈ 2.5 mJy/beam. The image cubes for each pointing were collapsed to a single plane containing only “significant” pixels and all pixels within 8 cells of significant pixels (see Fig. 2d). These were the brightest points in each image plane which was in excess of 6 times the off-source RMS and more than 0.15 times the brightest pixel in the channel image. Maser candidates were selected from the combined, collapsed cubes and elliptical Gaussians fitted. Note, this procedure will select continuum as well as maser candidates. Maser candidates were then tested using the spectrum extracted at the appropriate location from the combined spectral cube (see Fig. 2d). Spectral features were accepted if the channel with the highest flux density was in excess of 5 times the RMS of the other channels.

3. Results

Figure 1a reveals a color coded distribution of 356 methanol sources found in the region between Galactic longitude $-30' < l < 36'$ and latitude $-12' < b < 6'$. The size of each methanol source is proportional to the line flux of each source. The list of methanol sources of Table 1 in 10 columns gives: the source number, Galactic coordinates, the spatially integrated line flux, the center velocity, the lower limit to the brightness temperature (T_b) estimated from the maximum value in the spectrum interpolated at the fitted centroid of the spot in the collapsed image, the fitted values of the angular size and references. Given the large channel width (16.6 km s^{-1}), we can only identify maser candidates by their high estimated T_b , without information on the linewidths. For unresolved point sources, the line flux ranges between 0.19 and $468.31 \text{ Jy km s}^{-1}$, corresponding to brightness temperatures ranging between $T_b=8.5\text{K}$ and $2.1 \times 10^4\text{K}$, respectively. Typical masers have linewidths that are one to two orders of magnitudes smaller than the channel width we used, thus these sources could be much brighter if measured with smaller channel widths. As for sources with low brightness temperature, it is possible that these weak sources trace thermal methanol gas. However, thermal emission is generally spatially extended and the present snapshot survey does not have the sensitivity to detect extended emission on a scale $\geq 22''$. To test that bright sources in Table 1 include previously detected masers, we compare our sources with those of Sjouwerman et al. (2010; hereafter SPF) who had spectroscopically identified 36.2 GHz masers in the 50 km s^{-1} molecular cloud. SPF tabulates ten methanol masers (number 10, 6, 7, 8, 9 and 4 in their Table 1) ranging in brightness temperature $6.6 \times 10^4 < T_b < 2.3 \times 10^6\text{K}$. Six of the brightest sources coincide with sources that are detected in our survey (number 160, 164, 165, 167, 168, 169 in our Table 1) having similar LSR velocities. These spatial and spectral coincidences confirm maser candidate identification of bright sources in our survey.

Figure 1b shows the distribution of all detected methanol sources with their peak velocities superimposed on a grayscale continuum image of the Galactic center at 5 GHz. The peak velocities are accurate to within 10 km s^{-1} and can not identify multiple velocity components. Prominent radio continuum sources Sgr A, the nonthermal vertical and thermal arched filaments of the radio Arc, Sgr B1 and Sgr AC (the region between Sgr A and Sgr C) are labeled. The largest concentration of maser candidates lies in Sgr AC near $l \sim 40'$ and the radio Arc near $l \sim 0.1^\circ - 0.2^\circ$. We note a total of 200 and 150 sources distributed between $-0.5^\circ < l < 0^\circ$ and $0^\circ < l < 0.5^\circ$, respectively, suggesting an asymmetry with respect to Galactic longitude. We divide the source list into strong or weak maser candidate sources with line fluxes greater than or less than 10 Jy km s^{-1} ($T_b \sim 446\text{K}$ for unresolved sources), respectively. This threshold is selected because the gas temperature in the CMZ is much less than 446K . Figure 1c shows the distribution of all methanol maser candidates superimposed on a grayscale $24\mu\text{m}$ image showing similar asymmetry in terms of the number of YSO candidates (Yusef-Zadeh et al. 2009). This implies that star formation processes may be contributing to the origin of this asymmetry.

To examine the relationship between CH_3OH (36.2 GHz) maser candidates and dust emission, Figure 2a and 2b show the distribution of weak and strong methanol emission superimposed on the distribution of dust clouds at $850\mu\text{m}$, respectively (Pierce-Price et al. 2000). Methanol sources generally follow the “bow-tie” dust layer which runs parallel to the Galactic plane. The brightest methanol sources in Figure 2b show a good correlation of maser candidates and dust emission from the CMZ. To examine the central region of the CMZ in more detail, Figure 2c views the distribution of weak maser candidates superimposed on a grayscale image of SiO (2-1) line emission map (Tsuboi et al. 2011). Figure 2d shows the spectrum of a representative maser candidate and a collapsed image showing the distribution of bright sources in G0.13-0.13. A correlation between methanol maser candidates and SiO line emission suggests that the chemistry in producing enhanced methanol and SiO line emission is similar. This is interesting because the abundance of SiO produced in the ambient gas is too low, thus grain surface chemistry is needed to enhance the abundance of both SiO and CH_3OH throughout the Galactic center. In the following, we briefly discuss the distribution of methanol sources toward four Galactic center molecular clouds.

The 50 km s^{-1} Cloud: The 50 km s^{-1} M-0.02-0.07, is physically interacting with an expanding shell of the Sgr A East SNR G0.0+0.0 (e.g., Tsuboi et al. 2011). The presence of OH (1720 MHz) masers at the site of the interaction suggests that the abundance of OH is enhanced behind a supernova shock driving into the molecular cloud (Yusef-Zadeh et al. 1999; Wardle 1999). Figure 3a shows contours of SiO (2-1) line emission superimposed on a 5 GHz continuum image. The crosses represent the positions of 18 CH_3OH (36.2 GHz) maser candidates detected toward this cloud. The peak velocities, which are drawn next

to the position of individual maser candidates, range between 20 and 50 km s⁻¹ with the exception of one source showing a peak velocity of -133 km s⁻¹. The largest concentration of maser candidates coincide with a region where SiO (2-1) emission is strong but are offset by $\sim 30''$ (1.2 pc) from the compact HII regions. The circumnuclear ring orbiting Sgr A* lies to the west of the 50 km s⁻¹ cloud in Figure 3a and shows a lack of CH₃OH (36.2 GHz) maser candidates (see also SPF 2010). This result is consistent with CH₃OH (96 GHz) observations of the inner 10' of the Galactic center by Stanković et al. (2007), who suggest that strong UV radiation from young stellar clusters at the Galactic center is responsible for the destruction of methanol in the circumnuclear ring.

The 20 km s⁻¹ Cloud Another prominent Galactic center molecular cloud within four arcminutes of Sgr A* is the 20 km s⁻¹ molecular cloud M-0.13-0.08. Figure 3b shows contours of SiO (2-1) line emission from this cloud superimposed on a grayscale 5 GHz continuum emission. Maser Candidates are mainly concentrated in the region where SiO (2-1) line emission peaks having velocities ~ 20 and ~ 0 km s⁻¹ to the north and south of the cloud, respectively. The distribution of SiO (2-1), CH₃OH (36.2 GHz) and CH₃OH (96 GHz; Stankovic et al. 2007) are remarkably similar to each other suggesting that the abundance of SiO and CH₃OH in the gas phase are enhanced. A circular-shaped compact HII region Sgr A-G lies to the north and two extended nonthermal filaments Sgr A-E (G359.88-0.08) and Sgr A-F (G359.90-0.06) lie to the south. Both nonthermal filaments have X-ray counterparts showing a nonthermal spectrum (Sakano et al. 2003; Yusef-Zadeh et al. 2005), perhaps due to upscattering of far-infrared photons from dust emission of the 20 km s⁻¹ cloud by the relativistic electrons in the radio filaments.

G0.13-0.13 This cloud lies along the nonthermal filaments of the radio Arc near $l \sim 0.2^\circ$, the most prominent network of magnetized filaments in the Galactic center. The kinematics of CS line emission from G0.13-0.13 suggests an expansion of molecular gas into the nonthermal filaments (Tsuboi et al. 1997). Figure 3c shows the distribution of CH₃OH (36.2 GHz) emission from this cloud. Like the 50 and 20 km s⁻¹ molecular clouds, 45 maser candidates with velocities that range between 0 and 50 km s⁻¹ appear to trace the distribution of SiO (2-1) line emission with similar velocity. We also find three high velocity maser candidates at the eastern and western boundaries of the cloud. This cloud has recently been studied in detail showing compelling evidence for the interaction of molecular gas with nonthermal electrons (Yusef-Zadeh et al. 2012).

G0.25+0.01 G0.25+0.01 is a quiescent giant molecular cloud that coincides with the darkest cloud at mid-IR wavelengths in the so-called “Dust Ridge” (Lis & Carlstrom 1994). This cloud has a mass of $1.4 \times 10^5 M_\odot$ and exhibits little star formation (Lis and Carlstrom 1994; Immer et al. 2012). Figure 3d shows the spatial distribution of CH₃OH (36.2 GHz) maser

candidates and are represented as crosses with corresponding velocities superimposed on a $24\mu\text{m}$ image. Contours of SiO (2-1) line emission are also superimposed on Figure 3c. Like the above discussed clouds, maser candidates in G0.25+0.01 follow the distribution of SiO (2-1) and dust emission. There are no signatures of high mass star formation in this cloud, such as compact HII regions excited by OB stars, CH_3OH (6.6 GHz) masers, or shocked molecular outflows associated with protostars.

4. Discussion

The distribution of methanol emission throughout the Galactic center raises an important question: what is the mechanism by which methanol molecules are released off dust grains to enhance its abundance in the gas phase over such a widespread region. The tight correlation between SiO and CH_3OH emission suggests that grain surface chemistry is responsible for their production. Methanol is formed by hydrogenation of CO on interstellar grains at temperatures of 10-20K (Watanabe and Kouchi 2002) and is released into the gas phase by heating provided by UV radiation, by shocks due to cloud-cloud collisions, and by protostellar outflows. These processes are known to be important in star forming regions where hot molecular cores are formed and in cloud-cloud collisions where shocks drive into clouds. UV radiation can be important to release methanol but it is not possible to produce widespread methanol emission from dense, self-shielded Galactic center molecular clouds. The difficulty with large-scale shocks produced by cloud-cloud collisions is that methanol maser candidates are seen deep within dense giant molecular clouds and these shocks are most effective at the surface of clouds where the interaction takes place. Shocks can be generated locally in star forming sites. However, with the exception of Sgr B2, there is no evidence for widespread on-going star formation throughout the CMZ. The four giant molecular clouds that were discussed previously are examples in which on-going massive star formation has low efficiency (e.g., Immer et al. 2012). A more detailed discussion of additional issues related to enhanced SiO abundance in the Galactic center is discussed elsewhere (Yusef-Zadeh et al. 2013).

Instead, enhanced cosmic rays in the Galactic center interacting with molecular clouds provide a mechanism for globally enhancing the abundance of methanol. Recent large-scale studies indicate that the cosmic ray ionization rate over the inner few hundred pc is 10^{-15} to 10^{-14} s^{-1} , which is about one-to-two orders of magnitude larger than in the Galactic disk (Yusef-Zadeh et al. 2012; Ao et al. 2012). Induced photodesorption by cosmic rays traverse a molecular cloud and collide with, dissociate, ionize and excite Lyman and Werner transitions of H_2 (Prasad and Tarafdar 1983; Roberts et al. 2007). The FUV emission resulting from

these interactions can heat dust grains and evaporate methanol. There are other mechanisms that can evaporate methanol but total desorption of icy mantles, in a shielded environment, could only be explained by high rates of cosmic ray ionization (Roberts et al. 2007).

LVG modeling of CH_3OH emission from the inner 30pc of the Galactic center at 96 and 242 GHz requires a two-component model (Stanković, et al. 2007). The H_2 density and temperature are $n = 10^4 \text{ cm}^{-3}$ and $T \sim 90\text{K}$ in the warm phase with column density $N_{\text{CH}_3\text{OH}} \sim 2.6 \times 10^{15} \text{ cm}^{-2}$, whereas in the cold phase, $N_{\text{CH}_3\text{OH}} \sim 8 \times 10^{15} \text{ cm}^{-2}$ is estimated for $n = 5.5 \times 10^6 \text{ cm}^{-3}$, $T = 15\text{K}$ (Stanković, et al. 2007). Typical column densities of H_2 toward Galactic center clouds is 10^{23} to 10^{24} cm^{-2} , thus the abundance of methanol ranges roughly between 10^{-7} to 10^{-9} in these two phases. To explore the effect of high cosmic-ray ionization rates on the chemistry of the gas, we use a gas-grain time dependent chemical model, UCL-CHEM, to investigate the abundance of different species and compare them with observed values (Viti et al. 2004). This model initially follows the collapse of a prestellar core, and subsequently the warming and evaporation of grain mantles due to either the increase of temperature and/or an enhanced cosmic ray ionization rate. Given that $T_{\text{dust}} \leq 30\text{K}$, thermal evaporation is insignificant in this model. Figure 4 shows the abundance of CH_3OH , SiO , OH and NH_3 , as a function of time, for a grid of models. These species are either produced on the surface of the grains (CH_3OH , NH_3), or undergo an enhancement due to the release of the parent species from the grain mantles (SiO , OH). In these models, we varied the density from 10^4 cm^{-3} to 10^6 cm^{-3} and the cosmic ray ionization rate from 5×10^{-16} to $5 \times 10^{-14} \text{ s}^{-1}$. The models presented in Figure 4 give suitable CH_3OH abundances before they are destroyed. It turns out that the very process that is responsible to enhance the abundance of methanol in gas phase also destroys it on a time scale $10^4 - 10^5$ years. Figure 4 shows that methanol for low cosmic ray ionization rates lasts longest for both high and low density gas. In other words, as the cosmic ray ionization rate decreases, the chemical time scale for destruction of methanol increases. Methanol is highly volatile at high cosmic ray ionization rates, thus has a short destruction time scale. This is somewhat puzzling given that methanol emission is detected throughout the CMZ, which consists of several giant molecular clouds distributed within a couple of hundred pc. One possibility to account for this behavior is that methanol is constantly being replenished, thus increasing the destruction time scale. The reformation of methanol on the surface of dust grains can occur by the cold and dense component of the gas observed in the CMZ (Hüttmeister et al. 1998) during which methanol is being ejected from grain surfaces by cosmic rays. Other hydrogenated species do not get destroyed as fast as methanol in this picture. The other possibility is that we may be seeing a relatively short lived phase of the gas. This is because the medium is clumpy with several cores at different ages. Both these possibilities will be investigated theoretically in more detail elsewhere.

In summary, we carried out a survey of the Galactic center which resulted in the discovery of a large number of probable methanol masers at 36.2 GHz. These maser candidates were detected as part of continuum observations at 35 GHz. We found a strong correlation of maser candidates and molecular gas distribution in the central molecular zone. The identification of methanol emission as maser lines needs to be further investigated because of the poor spectral resolution employed in the continuum settings. While maser features are much narrower in frequency than our single channel width, we can put a lower limit on the brightness temperature of our maser candidates. It is possible that detected maser candidates have broad linewidths because they arise in molecular clouds with large linewidths or are contaminated by cluster of masers with different velocities. Future spectral line measurements will be able to distinguish thermal and maser emission.

We thank the referee for useful comments. This research is supported in part by grant AST-0807400 from the NSF the National Science Foundation.

REFERENCES

- Ao, Y., Henkel, C., Menten, K. M. et al. 2012, A&A, in press (arXiv1211.7142A)
- Hüttemeister, S., Dahmen, G. Mauersberger, R. Henkel, C., Wilson, T. L. & Martin-Pintado, J. 1998, A&A, 334, 646
- Immer, K., Menten, K. M., Schuller, F. & Lis, D. C. 2012, A&A, 2012, A&A, 548, 120
- Jones, P. A., Burton, M. G., Cunningham, M. R. et al., 2012, MNRAS, 419, 2961
- Lis, D. C. & Carlstrom, J. E. 1994, ApJ, 424, 189
- Martin, C. L., Walsh, W., Xiao, K. et al. 2004, ApJS, 153, 395
- Martin-Pintado, J., de Vicente, P., Fuente, A. & Planesas, P. 1997, ApJ, 482, L45
- Molinari, S., Bally, J., Noriega-Crespo, A., et al. 2011, ApJ, 735, L33
- Oka, T., Geballe, T. R., Goto, M., Usuda, T., & McCall, B. J. 2005, ApJ, 632 882
- Pierce-Price, D., Richer, J. S., Greaves, J. S., *et al.* 2000, ApJ, 545, 121
- Prasad, S. S. and Tarafdar, S. P. 1983, ApJ, 267, 603
- Riquelme, D., Bronfman, L., Mauersberger, R., et al. 2010, A&A, 523, A45

- Roberts, E., Rawlings, J. M. C., Viti, S. & Williams, D. A. 2007, MNRAS, 382, 733
- Sjouwerman, L. O., Pihlström, Y, M. and Fish, V. L. 2010, ApJ 710, L111
- Sakano, M., Warwick, R. S., Decourchele, A. & Predhel, P. 2003, MNRAS, 340, 747
- Stanković, M., Seaquist, E. R., Mühle, S., Leurini, S. & Menten, K. M. 2007, Molecules in Space and Laboratory, meeting held in Paris, France, May 14-18, Eds: J.L. Lemaire & F. Combes
- Tsuboi, M., Tadaki, K., Miyazaki, A. & Handa, T. 2011, PASJ, 63, 763
- Tsuboi, M., M., Ukita, N., & Handa, T. 1997, ApJ, 481, 263
- Viti, S., Collings, M. P., Dever, J. W. et al. 2004, MNRAS, 354, 1141
- Watanabe, N. & Kouchi, A. 2002, ApJ, 571, L173
- Voronkov, M. A., Brooks, K. J., Sobolev, A. M. et al. 2006, MNRAS, 373, 411
- Wardle, M. 1999, ApJ, 525, L101
- Yusef-Zadeh, F., Hewitt, J. W., Arendt, R. G. et al. 2009, ApJ, 702, 178
- Yusef-Zadeh, F., Goss, W. M., Roberts, D. A. et al. 1999, ApJ, 527, 172
- Yusef-Zadeh, F., Hewitt, J., Wardle, M. et al. 2012, ApJ, 762, 33
- Yusef-Zadeh, F., Wardle, M., Munro, M., Law, C. & Pound, M. 2005, AdSpR, 35, 1074
- Yusef-Zadeh, F., Wardle, M., Lis, D., Viti, S. et al. 2013, Journal of Physical Chemistry (submitted)

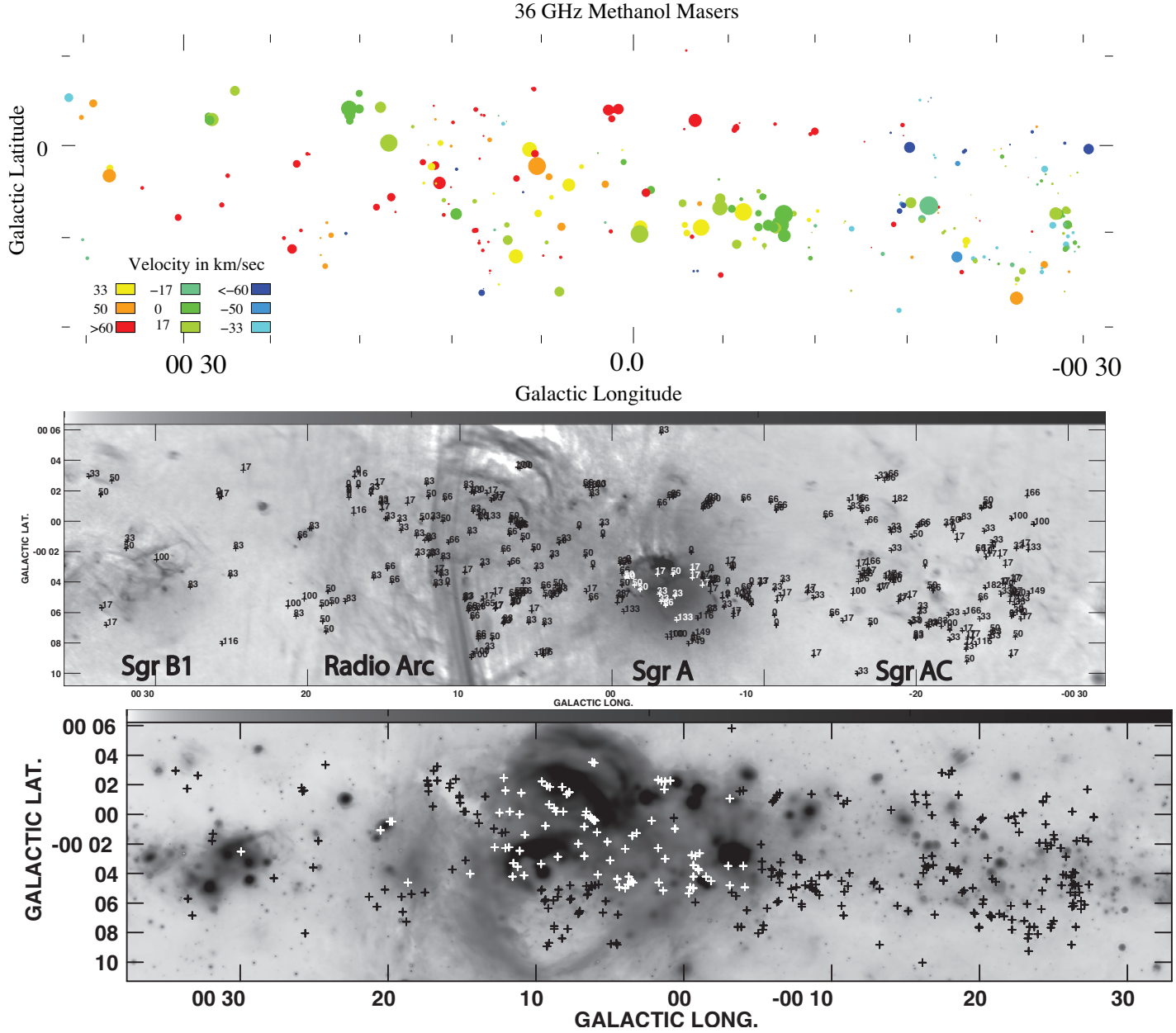


Fig. 1.— (a) *Top* Maser candidates in (l,b) coordinates. Color indicates velocity and the size of the symbol is proportional to the brightness. The line flux ranges between 0.19 to 468.31 Jy km s⁻¹. (b) *Middle* Methanol sources, with their velocities in km s⁻¹, (crosses) superimposed on a grayscale 5 GHz image (grayscale flux -0.1 to 300 mJy beam⁻¹). (c) *Bottom* Similar to (b) except a 24 μ m image (grayscale range 0 to 8; Yusef-Zadeh et al. 2009).

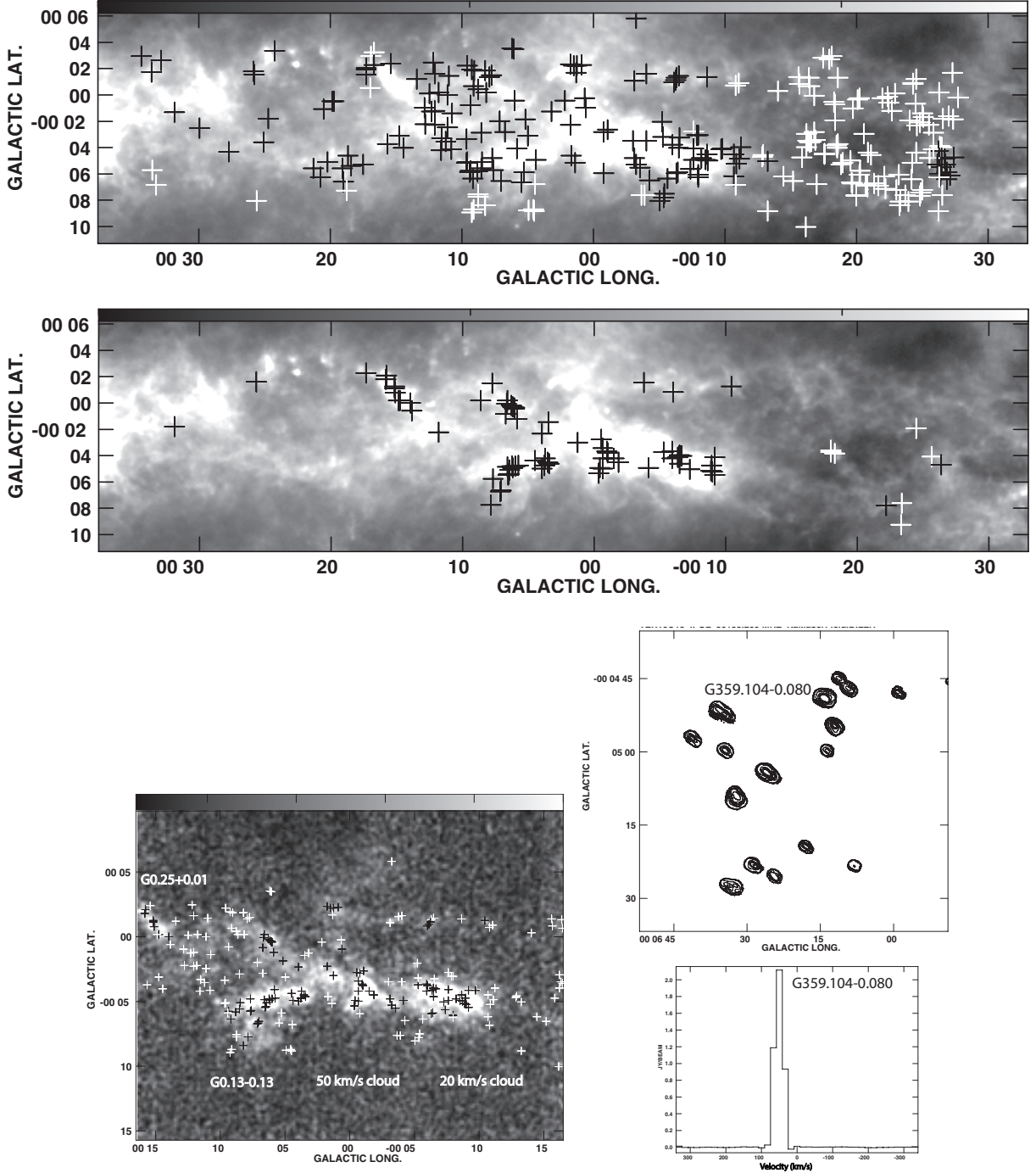


Fig. 2.— (a) *Top* Weak maser candidates (plus signs) on an $850\mu\text{m}$ map (grayscale range 0 to 5; Pierce-Price et al. 2000). (b) *Middle* Identical to (a) except bright maser candidates are shown. (c) *Bottom Left* All maser candidates on a map of SiO (2-1) line emission integrated between -152 to 197 km s^{-1} (grayscale range 0 to 5; Tsuboi et al. 2011). (d) *Bottom Right* A smoothed sample spectrum of a bright maser candidate G359.204-0.080 (source 113 in Table 1) in G0.13-0.13 and a collapsed 36.2 GHz image of G0.13-0.13. Contour levels are $(0.1, 0.15, 0.2, 0.25, 0.5, 0.75, 1, 1.5, 2.5, 3.5, 4.5) \times 0.5 \text{ Jy}$ per fitted beam size shown in Table 1).

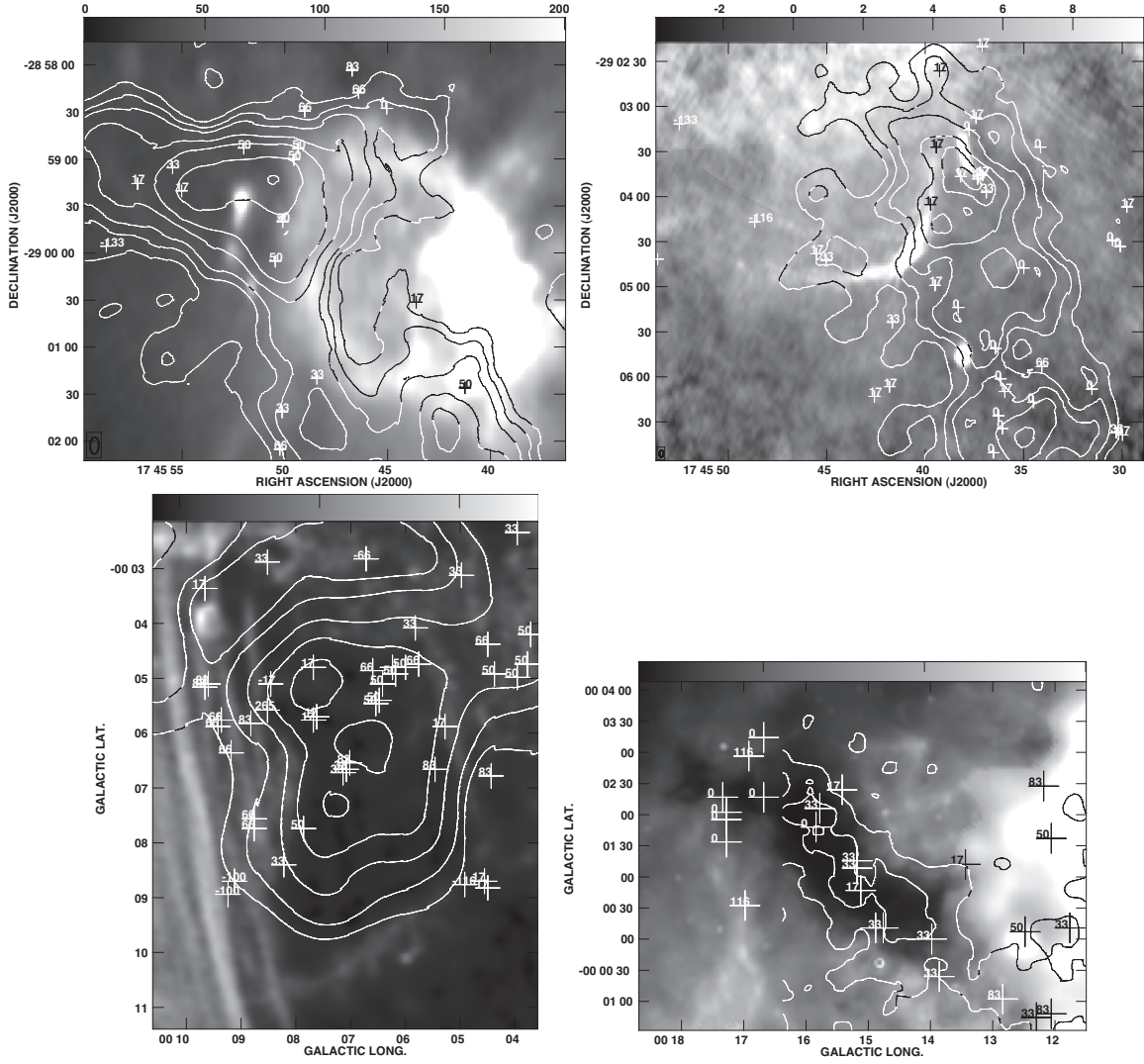


Fig. 3.— (a) *Top Left* CH₃OH (36.2 GHz) maser candidates (crosses) and LSR velocities on the shell-type SNR G0.0-0.0 image and its four compact HII regions. Contours of SiO (2-1) line emission integrated between 0 and 50 km s⁻¹ on the grayscale 5GHz image. (b) *Top Right* Similar to (a) except the 20 km s⁻¹ molecular cloud. (c) *Bottom Left* Contours of CS (1-0) line emission integrated between 0 and 50 km s⁻¹ from G0.13-0.13 with a resolution of 45'' (Tsuboi et al. 1997) on a 1.4 GHz image (grayscale range -9.4 to 128) Contour levels are 2, 4, 6, 8 and 10 km s⁻¹ K (T_A^{*}). (d) *Bottom Right* CH₃OH (36.2 GHz) maser candidates and contours of SiO (2-1) line emission on a 24μm map of G0.25+0.01 (grayscale range 0.11 to 1.5).

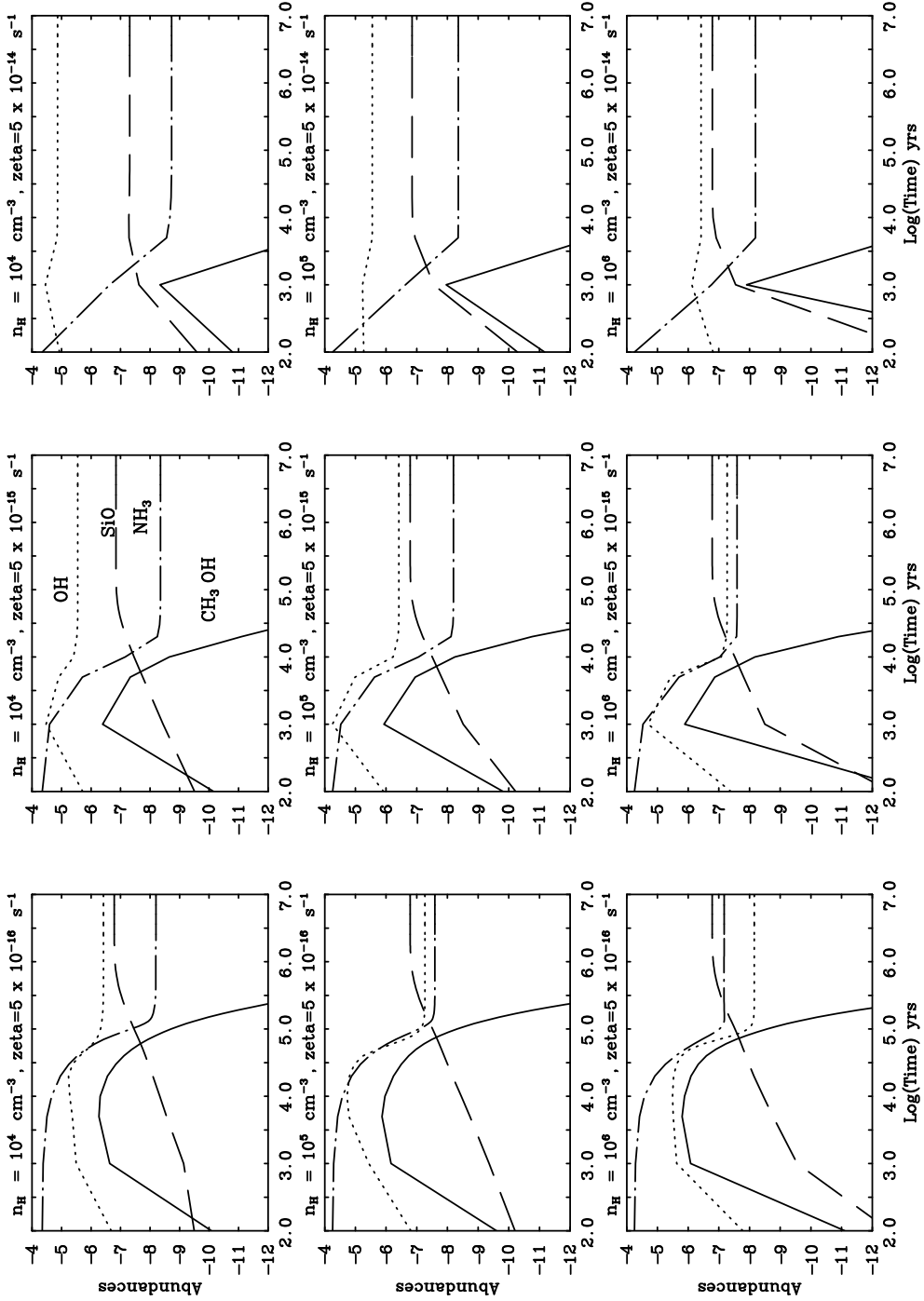


Fig. 4.— The abundance of CH₃OH, OH, NH₃ and SiO as a function of time in years for different values of cosmic ray ionization rate and molecular gas density using the UCL_CHEM time-dependent gas-grain chemical model (Viti et al. 2004).

Table 1. Detected CH₃OH Sources in the Survey

Source	G. long °	G. lat °	Flux Jy km s ⁻¹	Vel km s ⁻¹	T _B °K × 10 ²	Fit Major "	Fit Minor "	PA °	Ref.
1	0.57307	0.04923	7.32	-33.2	63.14 ± 12.60	6.00	0.66	3.7	
2	0.56038	0.02935	3.74	49.7	24.77 ± 4.38	6.00	0.86	2.9	
3	0.55883	-0.09493	2.00	-16.6	23.00 ± 4.17	2.27	1.31	3.8	
4	0.55429	-0.11371	2.63	-16.6	29.65 ± 4.94	2.24	1.35	5.2	
5	0.54816	0.04345	6.57	49.7	44.01 ± 6.30	6.00	0.85	4.7	
6	0.53183	-0.02997	11.49	49.7	51.91 ± 6.19	6.00	1.26	3.3	
7	0.53134	-0.02220	5.67	33.2	51.40 ± 7.58	3.73	1.01	0.2	
8	0.49866	-0.04223	2.68	99.5	33.00 ± 5.07	2.62	1.06	4.3	
9	0.46208	-0.07243	5.55	82.9	63.26 ± 5.93	2.63	1.14	-0.4	
10	0.43104	0.03018	6.49	0.0	52.39 ± 6.99	4.92	0.86	2.7	
11	0.43031	0.02641	8.13	0.0	55.03 ± 6.55	5.37	0.94	1.9	
12	0.42780	0.02715	11.42	16.6	89.83 ± 8.74	5.05	0.86	1.9	
13	0.42732	-0.13414	0.35	-116.0	15.41 ± 3.06	1.19	0.65	196.1	
14	0.41767	-0.05960	3.98	82.9	41.43 ± 6.33	3.01	1.09	5.8	
15	0.41177	-0.02976	3.42	82.9	26.16 ± 4.88	4.56	0.98	-183.6	
16	0.40449	0.05625	8.29	16.6	49.28 ± 9.65	4.75	1.21	1.2	
17	0.35465	-0.09316	2.87	99.5	29.34 ± 5.14	2.55	1.31	-7.2	
18	0.34644	-0.10415	7.97	82.9	23.40 ± 3.37	6.00	1.94	-0.9	
19	0.34168	-0.01792	6.27	66.3	57.00 ± 3.18	2.87	1.31	-190.3	
20	0.33745	-0.08545	2.50	99.5	38.92 ± 5.08	1.94	1.13	-11.7	
21	0.33109	-0.00765	2.64	66.3	26.37 ± 3.20	3.08	1.11	0.3	
22	0.32893	-0.00808	1.36	82.9	15.82 ± 3.13	2.90	1.01	-10.8	
23	0.31756	-0.09318	1.13	49.7	17.90 ± 3.45	1.64	1.31	-199.4	
24	0.31721	-0.11052	1.14	49.7	17.83 ± 3.29	1.96	1.11	-24.4	
25	0.31270	-0.12153	4.42	49.7	83.72 ± 3.14	1.61	1.12	-12.1	
26	0.31129	-0.07745	1.97	49.7	23.52 ± 3.73	2.35	1.22	-26.0	
27	0.30683	-0.09038	4.17	49.7	81.35 ± 3.76	1.70	1.03	-13.3	
28	0.29177	-0.08839	2.17	-82.9	31.23 ± 3.35	1.90	1.25	7.5	
29	0.28870	0.03819	13.81	0.0	29.12 ± 5.41	6.00	2.70	-191.0	
30	0.28826	0.03358	3.90	0.0	53.23 ± 10.51	2.88	0.87	-1.4	
31	0.28790	0.02572	9.46	0.0	28.58 ± 5.07	6.00	1.22	1.2	
32	0.28778	0.03178	6.13	0.0	95.57 ± 8.96	3.38	1.00	-1.5	
33	0.28282	0.00865	3.58	116.0	35.65 ± 3.94	3.01	1.14	-9.1	
34	0.28200	0.04905	1.37	116.0	17.40 ± 2.48	2.99	0.90	-0.0	
35	0.27847	0.05379	5.77	0.0	44.92 ± 6.91	4.18	1.05	0.6	
36	0.27824	0.03784	7.63	0.0	91.57 ± 12.65	2.79	1.02	-4.2	
37	0.26411	0.03025	35.72	0.0	529.92 ± 18.02	2.53	0.91	-1.6	
38	0.26334	0.03499	17.44	33.2	203.29 ± 25.65	2.64	1.11	-3.8	
39	0.26076	-0.06171	5.56	82.9	43.47 ± 4.59	2.73	1.60	-2.8	
40	0.25660	0.03957	9.54	16.6	76.30 ± 9.94	3.68	1.16	4.2	
41	0.25344	0.02118	21.70	33.2	260.14 ± 26.66	2.74	1.04	-3.7	
42	0.25338	0.01865	20.38	33.2	161.11 ± 26.99	3.79	1.14	-8.4	
43	0.25160	0.01312	20.04	16.6	165.75 ± 11.84	3.33	1.24	-1.3	
44	0.24827	0.00324	15.15	16.6	127.00 ± 20.79	3.26	1.25	-191.3	
45	0.24654	0.00297	6.82	33.2	274.56 ± 39.00	3.77	1.25	5.1	

Table 1—Continued

Source	G. long °	G. lat °	Flux Jy km s ⁻¹	Vel km s ⁻¹	T _B °K × 10 ²	Fit Major "	Fit Minor "	PA °	Ref.
46	0.24592	-0.05180	37.88	66.3	99.69 ± 4.09	2.29	1.02	-4.0	
47	0.24153	-0.06674	1.36	66.3	22.41 ± 3.11	1.96	1.06	-12.4	
48	0.23342	-0.00047	32.02	33.2	497.48 ± 56.52	2.29	0.96	-2.1	
49	0.23106	-0.00998	24.26	33.2	88.54 ± 14.88	6.00	1.56	4.5	
50	0.22401	0.01991	2.53	16.6	28.20 ± 4.76	2.81	1.09	-1.5	
51	0.21364	-0.01632	5.03	82.9	19.89 ± 3.37	4.91	1.76	-174.9	
52	0.21266	-0.03738	2.03	33.2	25.03 ± 3.44	2.50	1.11	-6.9	
53	0.20839	0.00144	0.61	49.7	12.89 ± 2.58	1.93	0.84	-9.3	
54	0.20507	-0.02072	6.15	33.2	101.53 ± 4.52	2.25	0.92	-4.5	
55	0.20259	0.04108	1.17	82.9	13.55 ± 2.64	2.82	1.05	-4.1	
56	0.20142	-0.01971	1.48	82.9	84.07 ± 4.40	2.61	1.11	-0.7	
57	0.20089	0.02738	1.49	49.7	16.36 ± 3.00	2.69	1.16	-5.7	
58	0.20055	-0.03783	7.13	33.2	20.26 ± 3.67	2.35	1.06	0.7	
59	0.19687	-0.03728	10.58	82.9	94.06 ± 5.37	3.23	1.19	0.9	
60	0.19597	0.00333	4.64	33.2	39.76 ± 3.46	3.47	1.15	-2.6	
61	0.19254	-0.06985	2.82	82.9	23.88 ± 4.44	3.25	1.24	6.9	
62	0.19253	-0.05463	3.29	16.6	20.65 ± 3.84	4.28	1.27	4.4	
63	0.18750	-0.05862	1.07	82.9	22.75 ± 4.50	1.84	0.87	-20.5	
64	0.18532	-0.04157	0.96	82.9	21.43 ± 4.26	1.55	0.99	-0.5	
65	0.18500	0.00011	2.02	49.7	24.91 ± 3.38	2.56	1.08	0.3	
66	0.18302	0.02401	2.67	66.3	25.61 ± 3.33	3.49	1.02	1.0	
67	0.18011	-0.06884	9.86	0.0	37.17 ± 3.97	6.00	1.51	198.7	
68	0.17952	-0.02330	2.32	-66.3	27.16 ± 2.96	2.30	1.27	-6.4	
69	0.16140	-0.08581	3.77	82.9	49.32 ± 5.46	2.07	1.26	-3.4	
70	0.16114	-0.05576	3.52	16.6	23.70 ± 3.46	3.76	1.35	10.9	
71	0.16007	0.03726	3.81	82.9	30.73 ± 3.33	2.99	1.36	5.4	
72	0.15974	-0.08534	3.66	82.9	26.39 ± 4.59	2.68	1.84	219.0	
73	0.15677	-0.09824	2.31	66.3	27.06 ± 5.00	2.54	1.15	231.6	
74	0.15653	-0.09594	1.10	66.3	24.69 ± 4.82	1.50	1.01	-17.4	
75	0.15609	-0.01274	1.48	82.9	21.25 ± 2.61	2.17	1.10	261.6	
76	0.15451	0.03194	5.23	99.5	14.58 ± 2.33	3.14	1.17	251.8	
77	0.15415	-0.14875	1.57	-99.5	112.04 ± 4.12	2.02	0.79	225.6	
78	0.15293	-0.10582	2.55	66.3	29.40 ± 5.04	2.45	1.21	54.9	
79	0.15222	-0.14471	0.43	-99.5	12.36 ± 2.28	1.75	0.68	228.7	
80	0.15219	0.01044	1.05	82.9	24.69 ± 2.66	1.91	0.76	246.0	
81	0.15149	0.03119	1.97	82.9	33.26 ± 3.79	2.02	1.00	252.9	
82	0.14727	-0.09708	1.58	82.9	22.94 ± 3.20	2.06	1.14	234.6	
83	0.14591	0.00659	0.38	49.7	42.49 ± 7.24	2.29	1.25	73.0	
84	0.14583	-0.12922	1.50	66.3	40.17 ± 1.58	0.92	0.35	-133.8	
85	0.14560	-0.12644	3.56	66.3	23.01 ± 3.35	2.19	1.02	223.5	
86	0.14358	0.00306	35.02	66.3	294.05 ± 13.22	3.60	1.13	78.1	
87	0.14240	-0.09352	0.19	265.2	7.41 ± 1.48	1.62	0.54	233.6	
88	0.14191	-0.04806	1.60	33.2	24.72 ± 3.24	2.07	1.07	238.8	
89	0.14078	-0.08507	1.75	-16.6	36.02 ± 2.21	1.89	0.88	234.6	
90	0.13691	0.03107	1.43	-16.6	16.86 ± 3.29	1.95	0.86	251.6	

Table 1—Continued

Source	G. long °	G. lat °	Flux Jy km s ⁻¹	Vel km s ⁻¹	T _B °K × 10 ²	Fit Major "	Fit Minor "	PA °	Ref.
91	0.13659	-0.14041	0.83	33.2	29.08 ± 4.48	1.91	0.88	229.2	
92	0.13648	0.00287	2.34	132.6	27.91 ± 3.59	2.09	1.37	252.4	
93	0.13234	0.02286	2.87	-33.2	56.73 ± 3.91	2.11	0.82	67.6	
94	0.13061	-0.12955	19.32	49.7	38.86 ± 4.56	6.00	2.83	32.8	
95	0.12902	0.02518	0.49	-16.6	110.21 ± 6.75	6.00	1.58	242.9	
96	0.12883	0.02502	30.59	-16.6	59.84 ± 3.25	0.75	0.37	-93.3	
97	0.12849	-0.07990	30.90	16.6	74.86 ± 5.32	2.13	0.89	230.3	
98	0.12762	-0.09609	4.15	16.6	350.35 ± 10.84	2.49	1.21	40.0	
99	0.12743	-0.09518	8.15	16.6	113.85 ± 10.35	1.62	1.51	320.3	
100	0.11942	-0.11160	12.28	33.2	126.28 ± 23.12	2.39	1.39	227.8	
101	0.11876	-0.03267	5.22	66.3	54.16 ± 9.44	2.42	1.36	58.2	
102	0.11788	-0.11073	68.67	33.2	87.45 ± 15.63	6.00	4.47	255.2	
103	0.11669	-0.10904	1.33	82.9	17.11 ± 2.99	2.51	1.06	234.6	
104	0.11254	-0.01404	1.41	66.3	247.52 ± 21.43	2.30	1.06	61.8	
105	0.11200	-0.04660	17.67	-66.3	25.94 ± 2.99	1.85	1.00	237.9	
106	0.11066	-0.00078	40.61	66.3	700.63 ± 38.37	2.20	0.90	246.6	
107	0.11045	0.00267	62.20	49.7	201.28 ± 6.09	6.00	4.39	205.2	
108	0.10984	-0.08124	155.22	66.3	533.96 ± 69.07	3.49	1.14	236.6	
109	0.10925	-0.09108	43.97	49.7	241.20 ± 43.31	3.44	1.81	71.1	
110	0.10797	-0.08989	33.18	49.7	376.04 ± 63.78	2.20	1.37	56.0	
111	0.10729	-0.08458	161.85	49.7	1510.15 ± 19.73	2.56	1.43	55.2	
112	0.10535	-0.00312	12.79	33.2	179.19 ± 14.86	2.30	1.06	64.2	
113	0.10402	-0.08034	197.63	49.7	1783.81 ± 127.98	2.38	1.59	68.8	
114	0.10344	-0.08196	104.14	49.7	1004.45 ± 149.02	2.27	1.56	41.9	
115	0.10297	-0.00477	1.85	49.7	198.27 ± 34.46	2.06	1.50	247.5	
116	0.10273	0.05847	17.94	99.5	27.56 ± 4.53	2.52	0.91	77.5	
117	0.10087	0.05790	3.54	99.5	50.85 ± 4.92	2.45	0.97	72.8	
118	0.10077	-0.00734	166.60	66.3	640.39 ± 38.49	5.66	1.57	255.6	
119	0.10071	-0.00614	46.34	66.3	736.44 ± 49.00	1.99	1.08	64.4	
120	0.09995	-0.00756	20.52	66.3	429.80 ± 31.75	1.23	0.40	62.9	
121	0.09981	-0.08000	6.19	49.7	442.89 ± 51.45	1.84	0.86	234.1	
122	0.09785	-0.02001	15.48	49.7	205.16 ± 13.72	2.13	1.21	64.3	
123	0.09694	-0.06808	6.04	33.2	47.17 ± 9.21	2.34	1.87	223.1	
124	0.09613	-0.07940	53.96	66.3	258.23 ± 27.04	3.09	2.31	78.9	
125	0.09154	-0.11098	1.46	82.9	19.08 ± 2.96	2.12	1.23	235.3	
126	0.08815	-0.09775	2.98	16.6	48.30 ± 5.83	2.15	0.98	231.0	
127	0.08575	-0.03094	5.55	49.7	101.63 ± 6.65	2.12	0.88	67.4	
128	0.08339	-0.05188	3.48	33.2	56.37 ± 9.69	1.97	1.07	232.9	
129	0.08184	-0.14598	2.25	-116.0	30.14 ± 2.37	2.38	1.07	226.0	
130	0.07616	-0.14549	4.14	16.6	44.51 ± 5.50	2.54	1.25	233.2	
131	0.07527	-0.07269	8.31	66.3	215.12 ± 19.99	2.58	1.31	241.4	
132	0.07522	-0.14753	21.29	16.6	31.64 ± 5.07	3.56	2.52	-222.1	
133	0.07394	-0.11272	2.22	82.9	29.39 ± 2.84	1.91	1.35	229.4	
134	0.07324	-0.08184	6.75	49.7	168.02 ± 19.80	1.83	0.75	231.3	
135	0.06623	-0.08346	27.60	49.7	449.88 ± 45.72	2.16	0.97	235.7	

Table 1—Continued

Source	G. long °	G. lat °	Flux Jy km s ⁻¹	Vel km s ⁻¹	T _B °K × 10 ²	Fit Major "	Fit Minor "	PA °	Ref.
136	0.06567	-0.03929	11.02	33.2	202.25 ± 7.12	2.19	0.85	59.7	
137	0.06264	-0.07933	41.42	49.7	424.97 ± 54.89	2.19	1.52	55.7	
138	0.06264	-0.07933	41.40	49.7	424.83 ± 54.88	2.19	1.52	55.8	
139	0.06220	-0.06987	28.65	49.7	342.17 ± 31.17	2.15	1.33	59.7	
140	0.05921	-0.07542	42.88	49.7	417.09 ± 43.40	2.28	1.54	49.5	
141	0.05832	-0.02368	22.13	49.7	483.74 ± 11.51	1.86	0.84	242.4	
142	0.05747	-0.07676	100.26	33.2	1482.48 ± 36.40	2.20	1.05	232.2	
143	0.05258	-0.02065	3.69	33.2	85.68 ± 5.06	1.84	0.80	238.4	
144	0.03621	-0.00703	0.86	0.0	14.08 ± 2.57	2.08	1.00	233.3	
145	0.02881	0.03942	0.99	66.3	14.10 ± 2.74	2.47	0.97	73.4	
146	0.02861	-0.03854	5.99	49.7	88.81 ± 11.47	2.45	0.94	240.7	
147	0.02850	-0.07745	1.71	-16.6	29.24 ± 3.30	2.06	0.97	238.6	
148	0.02545	0.03683	9.25	82.9	110.31 ± 9.50	2.58	1.11	72.7	
149	0.02288	-0.08630	3.06	66.3	36.11 ± 5.23	2.58	1.12	231.5	
150	0.02208	0.02794	5.61	82.9	69.64 ± 8.60	2.20	1.25	75.4	
151	0.02084	0.03667	91.15	99.5	63.09 ± 6.50	2.38	1.16	254.0	
152	0.02055	-0.05013	5.10	0.0	109.47 ± 11.74	6.00	4.74	353.3	
153	0.01534	0.03769	8.91	82.9	146.81 ± 12.86	2.16	0.96	68.7	
154	0.01145	-0.00382	1.09	33.2	21.80 ± 2.47	2.09	0.82	240.5	
155	0.01023	-0.01611	4.80	0.0	57.24 ± 5.17	2.63	1.09	56.1	
156	359.99392	-0.08895	15.48	16.6	196.57 ± 13.58	2.36	1.14	58.7	
157	359.99307	-0.08222	11.83	33.2	157.88 ± 27.20	2.15	1.19	230.9	
158	359.99125	-0.04605	24.35	82.9	200.40 ± 13.24	2.15	1.93	45.5	
159	359.98948	-0.06961	36.55	49.7	4640.42 ± 9.75	2.15	1.18	54.9	
160	359.98945	-0.05699	344.67	66.3	334.04 ± 41.22	1.92	0.95	235.9	SPF 2010
161	359.98874	-0.08297	17.84	16.6	353.04 ± 22.55	2.60	1.36	47.1	
162	359.98733	-0.09945	0.62	-132.6	14.30 ± 2.30	1.89	0.78	224.4	
163	359.98725	-0.04716	7.12	66.3	133.69 ± 19.12	1.82	1.00	237.7	
164	359.98442	-0.06142	468.31	49.7	7260.27 ± 56.31	2.16	1.02	242.8	SPF 2010
165	359.98313	-0.06307	243.67	49.7	3847.74 ± 256.27	2.23	0.97	236.4	SPF 2010
166	359.98229	-0.04431	6.66	0.0	68.40 ± 8.44	2.60	1.28	69.3	
167	359.97477	-0.07051	238.62	49.7	4403.94 ± 198.13	1.99	0.93	234.3	SPF 2010
168	359.96946	-0.07529	270.76	49.7	3086.45 ± 127.20	2.27	1.32	243.3	SPF 2010
169	359.95024	-0.05775	6.46	16.6	94.22 ± 7.27	2.17	1.08	235.4	SPF 2010
170	359.94841	0.01754	4.89	66.3	20.95 ± 3.60	1.99	1.21	67.1	
171	359.94789	-0.07981	1.48	33.2	73.30 ± 11.92	1.98	1.15	54.6	
172	359.94634	0.09725	1.51	82.9	25.52 ± 4.66	1.81	1.12	72.7	
173	359.94603	-0.08819	5.47	33.2	49.17 ± 7.09	3.22	1.18	241.7	
174	359.94057	-0.09195	3.35	66.3	61.44 ± 3.28	2.07	0.90	237.2	
175	359.93894	-0.12680	1.51	-99.5	17.42 ± 2.43	2.43	1.22	231.4	
176	359.93748	0.02629	11.31	66.3	44.72 ± 5.65	4.57	1.89	105.7	
177	359.93498	-0.12659	1.67	-99.5	14.26 ± 2.56	2.48	1.61	19.4	
178	359.93353	0.02722	3.71	66.3	29.82 ± 5.68	1.81	0.79	71.7	
179	359.93280	-0.05830	1.25	49.7	22.49 ± 4.22	4.34	1.30	228.5	
180	359.93145	-0.08252	14.43	33.2	106.18 ± 9.84	2.92	1.59	41.8	

Table 1—Continued

Source	G. long °	G. lat °	Flux Jy km s ⁻¹	Vel km s ⁻¹	T _B °K × 10 ²	Fit Major "	Fit Minor "	PA °	Ref.
181	359.92907	-0.10853	0.87	-132.6	12.29 ± 2.18	2.10	1.15	60.3	
182	359.91572	-0.13387	1.98	-149.2	12.37 ± 2.01	4.63	1.18	218.8	
183	359.91330	-0.03368	1.68	0.0	33.61 ± 2.66	1.94	0.88	246.4	
184	359.91238	-0.06231	13.31	16.6	171.46 ± 20.79	2.41	1.10	62.9	
185	359.91212	-0.05326	8.94	16.6	76.44 ± 11.29	2.48	1.61	238.1	
186	359.91146	-0.13058	4.44	66.3	43.89 ± 2.87	2.52	1.37	54.6	
187	359.90982	-0.12498	2.12	-149.2	36.64 ± 2.39	2.04	0.97	232.8	
188	359.90637	-0.10605	3.74	-116.0	46.75 ± 2.36	2.60	1.05	53.3	
189	359.90143	-0.06112	33.62	16.6	193.26 ± 27.05	6.00	1.69	248.8	
190	359.90064	-0.07022	57.37	16.6	293.48 ± 43.29	2.43	1.61	257.3	
191	359.90017	-0.06338	6.42	0.0	65.62 ± 9.91	2.32	1.44	244.8	
192	359.89990	0.01417	64.23	82.9	94.25 ± 4.99	6.00	3.88	177.8	
193	359.89776	0.01630	4.44	82.9	81.03 ± 8.06	2.08	0.90	68.0	
194	359.89603	0.01909	5.45	66.3	36.40 ± 6.43	3.14	1.63	266.2	
195	359.89544	0.02174	7.71	99.5	16.47 ± 3.18	2.27	1.14	69.7	
196	359.89540	-0.09942	1.25	16.6	78.15 ± 7.19	2.34	1.44	68.4	
197	359.89370	-0.06916	87.53	16.6	466.54 ± 65.25	3.56	1.80	260.7	
198	359.89341	-0.09847	4.85	33.2	25.76 ± 4.22	3.99	1.61	76.2	
199	359.89247	0.02356	23.71	82.9	20.52 ± 4.00	1.95	0.82	252.4	
200	359.89216	-0.07664	8.91	16.6	322.48 ± 34.68	2.73	0.92	56.4	
201	359.89188	-0.06567	32.31	16.6	1128.26 ± 50.52	1.63	0.60	246.6	
202	359.89173	-0.06563	121.66	16.6	685.48 ± 53.46	4.21	1.44	82.0	
203	359.89166	-0.06671	0.96	33.2	237.82 ± 41.04	1.60	0.80	60.9	
204	359.89062	-0.05378	2.77	0.0	48.68 ± 4.57	2.16	0.90	240.8	
205	359.88871	-0.06663	15.40	33.2	219.32 ± 30.02	2.05	1.17	63.6	
206	359.87897	-0.08370	67.67	16.6	64.21 ± 8.61	6.00	6.00	-308.3	
207	359.87722	-0.09400	2.96	33.2	36.71 ± 5.75	2.15	1.28	232.5	
208	359.87322	-0.08219	6.97	0.0	74.28 ± 9.96	2.94	1.09	58.1	
209	359.87316	-0.06802	5.16	0.0	113.50 ± 12.33	1.94	0.80	238.7	
210	359.87288	-0.04584	3.45	16.6	38.97 ± 4.78	2.03	1.49	233.3	
211	359.86896	-0.05139	5.55	0.0	87.10 ± 6.00	2.20	0.99	59.3	
212	359.86736	-0.10064	0.77	16.6	34.22 ± 6.60	3.52	1.07	48.8	
213	359.86727	-0.05074	3.77	0.0	47.01 ± 6.83	2.04	1.15	243.4	
214	359.86726	-0.10397	3.23	16.6	23.94 ± 4.48	1.50	0.73	228.7	
215	359.86319	-0.08024	9.43	0.0	85.19 ± 16.18	1.97	1.92	57.6	
216	359.85787	-0.08236	8.12	0.0	88.36 ± 13.14	1.95	1.61	66.5	
217	359.85638	0.02244	0.86	66.3	25.21 ± 2.50	2.77	1.25	253.8	
218	359.85585	-0.07471	2.56	66.3	15.06 ± 2.25	1.99	0.98	238.0	
219	359.85547	-0.08292	9.34	16.6	101.81 ± 18.73	2.59	1.21	63.5	
220	359.85228	-0.08624	149.18	0.0	408.28 ± 0.49	6.00	2.08	80.6	
221	359.85105	-0.07944	15.12	0.0	161.34 ± 31.82	2.56	1.25	61.5	
222	359.84987	-0.08684	22.38	0.0	214.02 ± 32.45	2.48	1.44	52.8	
223	359.84749	-0.06893	10.98	0.0	88.10 ± 11.41	2.93	2.12	-86.6	
224	359.84692	-0.09060	16.02	0.0	194.83 ± 19.28	2.07	0.93	236.2	
225	359.83829	-0.06929	0.53	33.2	14.30 ± 2.10	1.84	0.69	242.6	

Table 1—Continued

Source	G. long °	G. lat °	Flux Jy km s ⁻¹	Vel km s ⁻¹	T _B °K × 10 ²	Fit Major "	Fit Minor "	PA °	Ref.
226	359.83730	-0.06854	4.39	16.6	89.22 ± 3.52	2.00	0.84	239.1	
227	359.82592	0.02142	37.72	66.3	139.44 ± 12.17	6.00	1.54	249.3	
228	359.82202	-0.07485	1.37	33.2	41.98 ± 3.54	2.39	1.11	233.6	
229	359.82190	-0.10264	3.26	0.0	20.19 ± 3.10	2.00	1.16	233.0	
230	359.82047	0.01241	3.54	66.3	39.66 ± 4.20	2.53	1.02	70.2	
231	359.82038	-0.11362	3.00	0.0	21.64 ± 2.12	2.94	1.90	211.6	
232	359.81900	-0.08750	0.50	16.6	13.02 ± 2.47	1.92	0.68	226.9	
233	359.81586	0.01507	6.22	66.3	20.33 ± 3.41	5.94	1.76	42.5	
234	359.81546	-0.08071	2.52	-16.6	42.04 ± 2.88	2.47	0.83	59.1	
235	359.81315	-0.06568	2.53	33.2	15.99 ± 2.47	3.51	1.54	220.9	
236	359.78621	-0.07778	0.61	33.2	12.47 ± 2.24	2.07	0.81	61.1	
237	359.78515	-0.07612	0.93	16.6	19.36 ± 2.07	2.01	0.82	235.2	
238	359.77925	-0.14674	1.28	16.6	14.88 ± 2.46	3.22	0.91	44.6	
239	359.77882	-0.08390	4.41	-33.2	40.03 ± 2.74	3.58	1.05	236.8	
240	359.76561	0.00464	0.91	66.3	15.82 ± 2.34	1.96	1.00	245.1	
241	359.75855	-0.10280	0.56	66.3	16.14 ± 2.12	1.66	0.72	238.1	
242	359.74707	-0.10923	3.12	-16.6	57.76 ± 2.20	2.17	0.85	234.6	
243	359.74042	0.02272	1.13	-116.0	14.10 ± 2.46	2.34	1.17	247.6	
244	359.73899	0.01358	1.40	-82.9	10.34 ± 1.95	2.83	1.63	242.1	
245	359.73609	-0.07928	4.24	99.5	44.91 ± 2.45	2.60	1.24	223.0	
246	359.73059	-0.16664	3.99	-33.2	74.02 ± 8.66	1.96	0.94	224.6	
247	359.73010	-0.04932	4.28	16.6	18.96 ± 3.52	1.86	0.96	246.5	
248	359.73005	-0.06570	0.99	-66.3	14.77 ± 2.02	6.00	1.65	65.5	
249	359.72813	-0.05850	3.36	-49.7	19.13 ± 3.21	3.00	2.00	234.1	
250	359.72710	0.02165	3.31	66.3	31.65 ± 2.27	2.98	1.20	250.3	
251	359.72605	-0.05994	4.47	-66.3	41.08 ± 2.82	2.46	1.51	232.7	
252	359.72604	0.01086	0.58	66.3	12.93 ± 1.96	1.80	0.85	248.8	
253	359.72377	-0.05948	1.24	16.6	22.02 ± 3.75	1.86	1.03	56.7	
254	359.71997	-0.04707	0.23	165.8	7.68 ± 1.46	1.41	0.71	239.5	
255	359.71976	-0.00115	9.43	-66.3	69.86 ± 3.07	3.27	1.41	70.7	
256	359.71863	-0.05738	9.27	16.6	184.25 ± 3.93	1.93	0.89	240.6	
257	359.71749	-0.11269	2.31	49.7	38.24 ± 2.11	2.17	0.95	231.0	
258	359.70932	0.04683	1.91	-33.2	13.99 ± 2.17	2.78	1.68	241.6	
259	359.70734	-0.07544	3.79	16.6	29.54 ± 4.12	2.53	1.73	22.5	
260	359.70725	-0.07365	6.22	-16.6	25.64 ± 3.94	3.65	2.27	-68.0	
261	359.70077	0.04532	0.36	-66.3	7.77 ± 1.46	1.87	0.85	250.0	
262	359.70041	-0.06189	24.31	16.6	485.33 ± 12.17	1.88	0.91	236.9	
263	359.70034	-0.06017	16.39	-16.6	83.65 ± 7.42	3.78	1.77	-79.6	
264	359.69811	0.04914	0.58	-66.3	12.55 ± 1.74	2.02	0.78	253.6	
265	359.69535	-0.06408	91.21	0.0	199.05 ± 19.10	5.36	2.92	40.7	
266	359.69505	-0.00900	1.40	-33.2	17.23 ± 2.99	2.27	1.22	66.6	
267	359.69393	-0.03167	0.99	-33.2	10.07 ± 1.85	2.62	1.28	43.6	
268	359.69368	-0.01172	1.57	-33.2	24.77 ± 2.60	2.14	1.01	63.6	
269	359.69215	-0.06432	1.61	16.6	33.73 ± 5.87	1.81	0.90	233.5	
270	359.69072	-0.06757	1.13	49.7	16.03 ± 2.77	2.13	1.13	236.5	

Table 1—Continued

Source	G. long °	G. lat °	Flux Jy km s ⁻¹	Vel km s ⁻¹	T _B °K × 10 ²	Fit Major "	Fit Minor "	PA °	Ref.
271	359.69037	-0.06198	2.13	66.3	13.26 ± 2.25	2.92	1.88	-105.4	
272	359.68993	0.02148	0.66	182.3	8.22 ± 1.58	2.25	1.22	244.4	
273	359.68591	-0.08802	2.36	16.6	29.54 ± 4.64	2.07	1.32	50.3	
274	359.68433	-0.08619	1.98	16.6	29.68 ± 4.47	2.13	1.07	231.6	
275	359.67418	-0.08344	1.71	16.6	16.55 ± 2.97	2.73	1.29	68.3	
276	359.67309	-0.11099	2.77	-33.2	27.40 ± 4.21	2.20	1.57	243.7	
277	359.67181	-0.11227	9.25	-49.7	48.11 ± 5.24	4.35	1.51	235.2	
278	359.67104	-0.01738	4.10	-49.7	29.03 ± 2.72	3.15	1.53	51.9	
279	359.66701	-0.12689	3.45	82.9	9.06 ± 1.78	1.60	0.50	236.0	
280	359.66696	-0.12769	0.21	82.9	10.57 ± 1.77	6.00	1.86	3.8	
281	359.66485	-0.00561	2.87	-66.3	26.70 ± 2.73	2.62	1.40	231.4	
282	359.66334	-0.00443	3.35	-66.3	13.43 ± 2.09	3.24	2.06	95.4	
283	359.66298	-0.10114	2.62	33.2	46.97 ± 2.88	2.30	1.06	229.8	
284	359.66214	-0.09612	6.43	33.2	14.26 ± 1.76	5.66	2.72	73.0	
285	359.65748	-0.04938	0.25	0.0	7.95 ± 1.51	1.41	0.75	241.2	
286	359.65518	-0.11404	3.51	-33.2	44.25 ± 3.51	2.28	1.19	232.2	
287	359.65331	-0.11655	3.79	16.6	19.83 ± 2.40	3.47	1.88	20.7	
288	359.65286	-0.11471	2.10	-16.6	31.73 ± 3.05	2.35	0.96	227.2	
289	359.65240	-0.07259	0.64	49.7	12.04 ± 2.04	2.00	0.91	235.2	
290	359.64844	-0.07564	0.82	66.3	13.57 ± 2.01	2.26	0.91	234.4	
291	359.64410	-0.11235	2.34	-33.2	14.27 ± 1.87	3.62	1.55	78.6	
292	359.63871	-0.11517	0.70	-99.5	13.09 ± 1.52	2.09	0.88	232.0	
293	359.63413	-0.00388	0.85	33.2	11.17 ± 2.08	2.69	0.97	69.2	
294	359.63116	-0.10315	2.10	-33.2	37.20 ± 2.01	2.05	0.94	229.2	
295	359.63046	-0.12960	19.33	-33.2	42.97 ± 3.54	6.00	2.56	64.7	
296	359.62961	-0.11936	1.77	0.0	30.20 ± 2.30	2.08	0.96	228.5	
297	359.62697	-0.00252	0.50	49.7	11.88 ± 1.70	1.85	0.78	241.6	
298	359.62601	-0.01054	3.28	0.0	13.32 ± 2.38	3.20	2.63	8.3	
299	359.62237	-0.02023	0.87	16.6	14.53 ± 2.87	2.60	0.79	72.6	
300	359.61799	0.00161	0.88	-82.9	15.81 ± 1.71	1.89	1.01	68.1	
301	359.61562	-0.12052	3.56	-16.6	41.22 ± 2.54	2.73	1.08	51.7	
302	359.61293	-0.10059	0.64	-165.8	10.24 ± 1.92	1.98	1.07	224.2	
303	359.61182	-0.14008	1.22	33.2	15.89 ± 3.05	2.22	1.18	217.4	
304	359.61137	-0.15415	11.32	49.7	30.14 ± 5.69	4.63	2.77	-172.5	
305	359.61073	-0.13502	4.14	16.6	35.20 ± 3.71	2.89	1.39	224.4	
306	359.60968	-0.12697	18.78	16.6	69.86 ± 4.38	4.10	2.24	235.8	
307	359.60539	-0.12674	5.37	16.6	36.27 ± 4.76	3.14	1.61	236.2	
308	359.60103	-0.13530	2.05	-116.0	29.30 ± 2.68	2.21	1.08	223.4	
309	359.59932	-0.03160	0.26	66.3	10.47 ± 1.94	1.65	0.51	249.4	
310	359.59745	-0.10733	0.93	-33.2	12.19 ± 1.58	2.23	1.17	61.4	
311	359.59571	-0.08651	1.44	66.3	24.90 ± 2.23	1.98	1.00	232.1	
312	359.59532	0.01449	2.42	-82.9	14.19 ± 1.77	4.05	1.44	43.5	
313	359.59509	0.01421	0.33	-82.9	15.38 ± 1.42	1.45	0.50	-97.0	
314	359.59207	-0.03232	33.69	16.6	661.85 ± 6.70	1.89	0.92	241.7	
315	359.59174	-0.01153	0.41	-33.2	10.62 ± 1.97	1.57	0.83	65.7	

Table 1—Continued

Source	G. long °	G. lat °	Flux Jy km s ⁻¹	Vel km s ⁻¹	T _B °K × 10 ²	Fit Major "	Fit Minor "	PA °	Ref.
316	359.59090	0.01987	0.79	49.7	13.68 ± 2.17	3.62	1.17	70.8	
317	359.59057	-0.07270	1.70	-182.3	10.37 ± 1.75	2.29	1.14	57.9	
318	359.59024	-0.03875	1.57	-16.6	36.16 ± 2.19	1.76	0.84	241.8	
319	359.58603	-0.03510	3.23	0.0	39.98 ± 3.98	1.96	1.01	242.2	
320	359.58557	-0.12764	2.32	-33.2	48.75 ± 3.84	2.22	1.02	232.1	
321	359.58532	-0.12387	2.00	-33.2	25.16 ± 2.94	2.19	1.24	235.3	
322	359.58314	-0.12013	5.98	49.7	66.68 ± 2.81	2.27	1.35	230.9	
323	359.58273	-0.02309	5.41	-33.2	113.19 ± 3.00	1.92	0.85	242.2	
324	359.58159	-0.02835	1.26	0.0	18.99 ± 3.25	2.00	1.13	64.7	
325	359.57500	-0.03812	1.59	16.6	27.08 ± 3.19	2.00	1.00	63.0	
326	359.57453	-0.08034	5.50	-33.2	36.01 ± 2.89	3.55	1.47	221.2	
327	359.57163	-0.06838	10.87	16.6	203.60 ± 3.63	1.96	0.93	235.1	
328	359.56911	-0.04780	8.74	16.6	14.62 ± 2.52	1.79	0.73	241.8	
329	359.56875	-0.06905	0.56	0.0	38.35 ± 5.11	4.50	1.73	254.9	
330	359.56357	-0.08833	2.03	16.6	34.29 ± 2.97	1.96	1.03	227.4	
331	359.56338	-0.07097	0.73	0.0	26.92 ± 4.42	2.14	1.10	61.4	
332	359.56268	-0.14744	1.86	16.6	10.99 ± 2.19	1.96	1.15	223.6	
333	359.56238	0.00319	4.32	-99.5	12.61 ± 1.95	5.24	1.16	66.8	
334	359.56205	-0.07962	2.80	-16.6	48.77 ± 6.82	2.11	0.93	235.8	
335	359.56173	-0.10442	2.24	0.0	59.33 ± 3.23	2.26	1.10	46.5	
336	359.56124	-0.06490	4.82	16.6	34.59 ± 4.62	3.55	1.77	47.5	
337	359.56105	-0.09965	6.36	-33.2	18.80 ± 3.16	6.00	1.46	243.4	
338	359.56024	-0.07788	4.22	0.0	201.35 ± 6.58	2.40	1.47	242.2	
339	359.55987	-0.10264	20.80	-16.6	39.73 ± 4.77	2.50	1.45	47.4	
340	359.55948	-0.07965	2.83	0.0	88.69 ± 8.18	2.30	1.25	236.9	
341	359.55939	-0.06581	7.47	16.6	54.88 ± 4.80	2.28	1.36	234.5	
342	359.55915	-0.09138	4.98	-33.2	43.55 ± 4.96	2.20	1.01	229.3	
343	359.55800	-0.12721	1.75	49.7	15.75 ± 2.61	2.52	1.51	41.9	
344	359.55656	-0.02985	0.75	33.2	12.25 ± 2.18	1.95	1.07	62.7	
345	359.55541	-0.08125	0.61	49.7	12.27 ± 2.17	1.88	0.91	236.7	
346	359.55400	-0.08780	2.10	-33.2	26.30 ± 3.26	2.39	1.14	227.5	
347	359.55224	-0.10681	0.84	-16.6	14.87 ± 2.97	1.57	1.23	221.6	
348	359.55190	-0.09791	3.44	0.0	49.21 ± 5.06	2.21	1.08	226.1	
349	359.54964	-0.02676	1.12	16.6	9.15 ± 1.79	2.63	1.59	-80.5	
350	359.54830	-0.10225	1.79	0.0	23.91 ± 2.92	2.37	1.08	225.7	
351	359.54553	0.02807	0.63	165.8	9.69 ± 1.75	2.30	0.96	68.4	
352	359.54356	-0.03096	0.59	132.6	12.23 ± 1.97	1.76	0.93	240.6	
353	359.54333	-0.07923	3.83	-149.2	20.59 ± 1.67	3.69	1.72	30.8	
354	359.53838	-0.00289	0.42	-99.5	104.52 ± 0.91	1.97	0.07	92.8	
355	359.53821	-0.00291	8.84	-99.5	124.24 ± 5.13	2.48	0.98	247.7	